Published for the International Glaciological Society

THIS MANUSCRIPT HAS BEEN SUBMITTED TO THE JOURNAL OF GLACIOLOGY AND HAS NOT BEEN PEER-REVIEWED.

Fracturing during freezing in salty ice: preliminary analysis using a low-cost model system

Journal:	*Journal of Glaciology*
Manuscript ID	JOG-2025-0023
Manuscript Type:	Article
Date Submitted by the Author:	25-Feb-2025
Complete List of Authors:	Cruz, Cody; University of Washington, Lipovsky, Bradley; University of Washington College of the Environment, Department of Earth and Space Sciences
Keywords:	Ice shelves, Ice/ocean interactions, Glaciological model experiments, Ice physics
Abstract:	The fracture properties of saline water ice play an important role in governing the mechanical behavior of sea ice, marine ice sheets, and icy planetary bodies. Here, we design a low-cost experimental system based on a simple observation: fractures form when freshwater is frozen in a plastic bag, but do not form when a small amount of NaCl salt (several g/L) is added before freezing. We attribute this brittle--ductile transition to the formation of a brine-filled pore space in the saline samples that inhibits the high water pressures required to generate hydrofracture. This interpretation is confirmed using in situ pressure measurements and dye tracing experiments. We develop a radially symmetric poroelasticity model where the freezing process is represented as a transformation strain. Together with experimental data, our model is able to constrain the sample permeability, which we find to at least 10^{-14} m^2 for samples with an estimated porosity in the range of 0.02 to 0.06. Our work offers an explanation of the observation that accreted marine ice stabilizes the Antarctic ice shelves.

Journal of Glaciology, Vol. 0, No. 0, 2025

Fracturing during freezing in salty ice: preliminary analysis using a low-cost model system

Cody Cruz,[1] Bradley P Lipovsky[2]

[1] *University of Washington, Department of Physics, School of Oceanography, Seattle, WA, USA*

[2] *University of Washington, Department of Earth and Space Sciences, Seattle, WA, USA*

Correspondence: Bradley P Lipovsky <bpl7@uw.edu>

ABSTRACT. The fracture properties of saline water ice play an important role in governing the mechanical behavior of sea ice, marine ice sheets, and icy planetary bodies. Here, we design a low-cost experimental system based on a simple observation: fractures form when freshwater is frozen in a plastic bag, but do not form when a small amount of NaCl salt (several g/L) is added before freezing. We attribute this brittle–ductile transition to the formation of a brine-filled pore space in the saline samples that inhibits the high water pressures required to generate hydrofracture. This interpretation is confirmed using in situ pressure measurements and dye tracing experiments. We develop a radially symmetric poroelasticity model where the freezing process is represented as a transformation strain. Together with experimental data, our model is able to constrain the sample permeability, which we find to at least 10^{-14} m^2 for samples with an estimated porosity in the range of 0.02 to 0.06. Our work offers an explanation of the observation that accreted marine ice stabilizes the Antarctic ice shelves.

INTRODUCTION

The hydromechanical properties of various salt-bearing water ices are important for a variety of topics in the Earth and planetary sciences. The Antarctic ice shelves are strengthened when sea water freezes onto the bottom of the ice shelf, particularly in suture zones (Craven and others, 2009; Jansen and others, 2013;

McGrath and others, 2014; Borstad and others, 2017; Kulessa and others, 2019). The way in which sea ice transfers heat, salt, nutrients, and momentum between the ocean and atmosphere is controlled by its hydromechanical properties (Maus and others, 2020). Icy planet surface morphology, chemical cycling, and habitability potential are affected by the flow of subsurface brines through a permeable icy matrix (Vance and others, 2016; Buffo and others, 2021; Wolfenbarger and others, 2022).

Laboratory hydromechanical testing of ice samples is notoriously difficult and as a result relatively few studies have carried out such work (see, for example, the review by Schulson and Renshaw, 2022, Section 6.2). One approach is to use model systems that are easier to work with and understand, yet may differ from the target system in certain aspects. Yuan and others (2024), for example, inject water into soft hydrogel specimens and document the resulting hydraulic fracture growth. Intermediate scale field experiments have the benefit of taking place in a controlled yet naturally occurring site (Fu and others, 2021). One of the few studies that has carried out actual hydraulic fracturing experiments in water ice is that by Chen and others (2019), who carried out tests aimed at simulating hydraulic fracturing phenomena in ice boreholes. Another approach is to combine microstructural imaging (McCarthy and others, 2007) with flow modeling (Maus and others, 2020), to calculate permeability numerically. Although accompanied with various strengths and weaknesses, traditional laboratory methods may be expensive in both material costs and personnel time.

We present a simple, reproducible model system for poroelastic fracture in salty ice samples. Our system consists of a sealed plastic bag that undergoes freezing. The novelty of our method is that the volume change during the phase transition is used to drive a pressure gradient that probes the hydromechanical properties of an incipient ice shell. We find that the inclusion of salt in our experiments inhibits ice fracture. We conclude with a discussion of relevant analytic models that describe the hydraulic fracturing in our setup.

METHODS

Basic experimental setup

We conducted freezing experiments in a thermally insulated SK-2101 Associated Environmental Systems Environmental Chamber (Figure 1). Although the environmental chamber was more sophisticated than typical consumer appliances, we note the general trend of results were initially obtained in a household freezer. A total of 80 experiments were performed in the environmental chamber over a range of constant ambient air temperatures between -5° C and -70° C. We estimate that the temperature set point had a

Fig. 1. The Associated Environmental Systems Environmental Chamber (Model SK-2101) with frozen ice sample, hollow aluminum stand, thermocouple temperature sensor, and pressure sensor with cable gland.

precision and accuracy of about 1° C. Water salinities were varied over a range between 0 and 7 g/L.

We put 1 L of tap water in 1-quart Ziploc brand plastic bags (specified dimensions 17.7cm x 18.8cm). In experiments with added NaCl salt, consumer-grade table salt was dissolved in the water by mixing. After manually squeezing the air out, the bags were sealed with the zip and placed in the environment chamber on a hollow aluminum stand with grating to promote air circulation. This latter step was done to promote freezing from the outside of the sample inwards. Experiments concluded roughly after the water was fully frozen, when the ice and ambient air reached thermal uniformity.

During some of our experiments, we recorded video using a Teslong NTS300 Industrial Borescope. The borescope was inserted through the environmental chamber's access port and positioned to record video and the access port was thermally insulated with foam.

Temperature and pressure measurement

For a subset of our experiments we collected data from MS5803-05BA temperature and pressure sensors. We inserted these sensors through the plastic on the top face of the bag before inclusion of water or salt. The bags were sealed around the four-strand sensor cable with hard-plastic glands. The cables were inserted into the environmental chamber through its access port. In experiments with sensors, the bags were positioned such that the cables did not deform the plastic. The sensors were positioned in the approximate center of the bags to ensure that the sensor took measurements of the last liquid water to freeze without distorting the geometry of ice growth. It was found that significant disruptions to the bag resulted in pathological sensor readings; these readings are not reported here. At the typical temperature and pressure conditions of the experiments, the sensors had systematic temperature and pressure errors of up to roughly ± 15 millibars and $\pm 0.25°$ C, respectively. We did not find a significant change in these statistics as a function of temperature.

Initial experiments used one sensor with an ESP8266 microcontroller. MicroPython was used to instruct the microcontroller to take temperature and pressure readings every 30 seconds. Further experiments used up to four pressure sensors with a Raspberry Pi Pico microcontroller. In this setup, each sensor took a reading every 15 seconds. In addition to a Mouser Electronics Multilayer Ceramic 0.1 μF capacitor and three size 080510KΩ Chanzon Chip Resistors, the temperature and pressure sensors were mounted to the surface of custom PCBs with gel solder. After bonding the components to the PCBs with a heating gun, they were placed in 3-D printed cases and potted with waterproof epoxy, leaving only the silicon-gel-coated sensor exposed.

Dye tracing

We performed a series of auxiliary experiments to determine whether brine was able to flow through the ice matrix. We inserted a one-way valve positioned at the center of the bag. This valve facilitated the injection of red dye into the remaining liquid when the ice had grown part of the way to the center.

RESULTS

Our most important result is that dissolved NaCl salt inhibits fracturing during freezing of water ice (Figure 2). This main result was first achieved using a consumer-grade kitchen freezer. More refined experiments, using the temperature controlled environmental chamber, yield quantitative relationships between temperature, salinity, and hydrofracturing. We generally found that our experiments in the environmental chamber were highly reproducible and the details of all experiments are listed in tables in the Supporting Information.

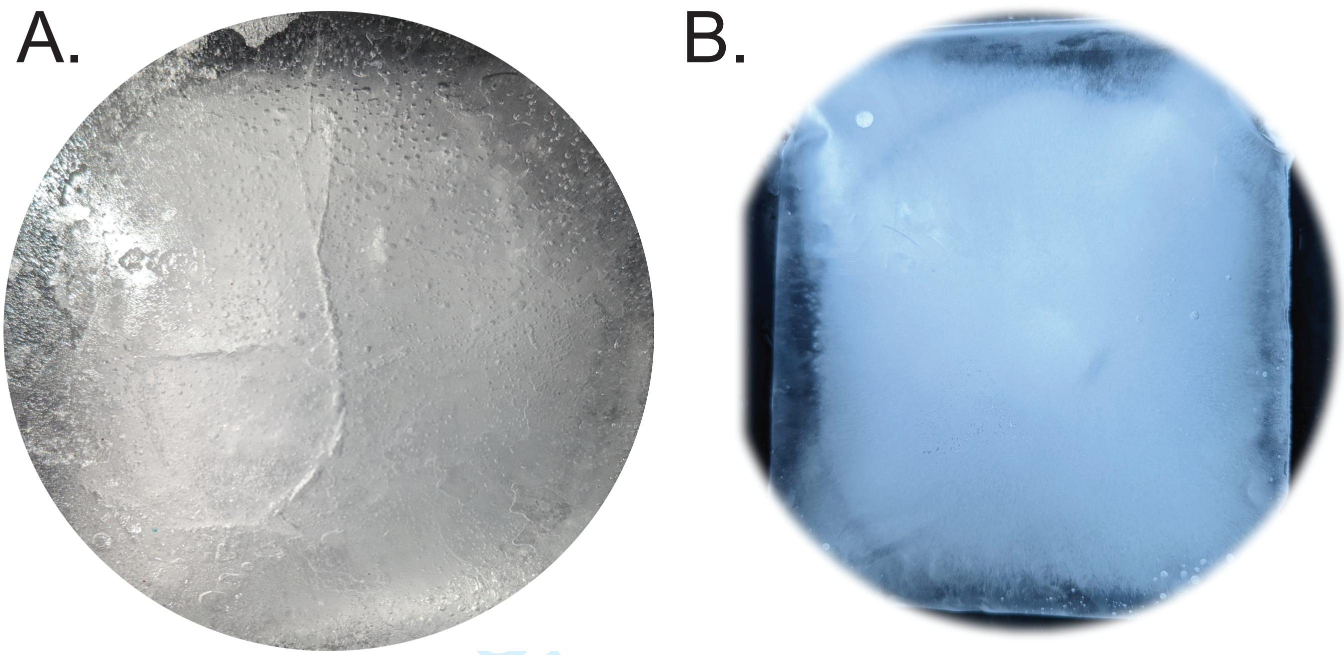

Fig. 2. A. Sample with fractures at set point temperature -30 °C and salinity 0.25 g/l (the image spans 1.7 cm). B. Sample without fractures at set point temperature -30 °C and salinity: 0.5 g/l (the image spans 2 cm). Note that the fracturing present at lower salinity (A) has been suppressed by increasing salinity (B).

Pressure sensor observations

Pressure sensors record a typical sequence of events (Figure 3). In the first hour or two of an experiment, there is little pressure change. Then, as the ice fronts progress towards the center of the bags, liquid pressure begins to rise. In both freshwater and saltwater experiments, water pressure peaks near the end of ice formation, at approximately 3500 millibar, as the remaining liquid expands by volume in the constrained space of the plastic bag. Both freshwater and saltwater experiments conclude with a pressure drop below atmospheric pressure that then diminishes, leaving the sample at atmospheric pressure.

The freshwater and saltwater experiments show a notable qualitative difference: the freshwater experiments experience rapid water pressure variations. The saltwater experiments, in contrast, show a smooth pressure time series. We confirmed using two simultaneously operating pressure sensors that these rapid pressure oscillations are not instrumental in origin. To further verify that the observed pressure fluctuations in freshwater samples are due to actual water pressure variations, we conducted an experiment where a sample was pulled from the environmental chamber prior to complete freezing. Inspection of the sample showed little ice growth on the sensors ahead of the main ice front, confirming that observed pressure fluctuations predominantly originate within the liquid phase.

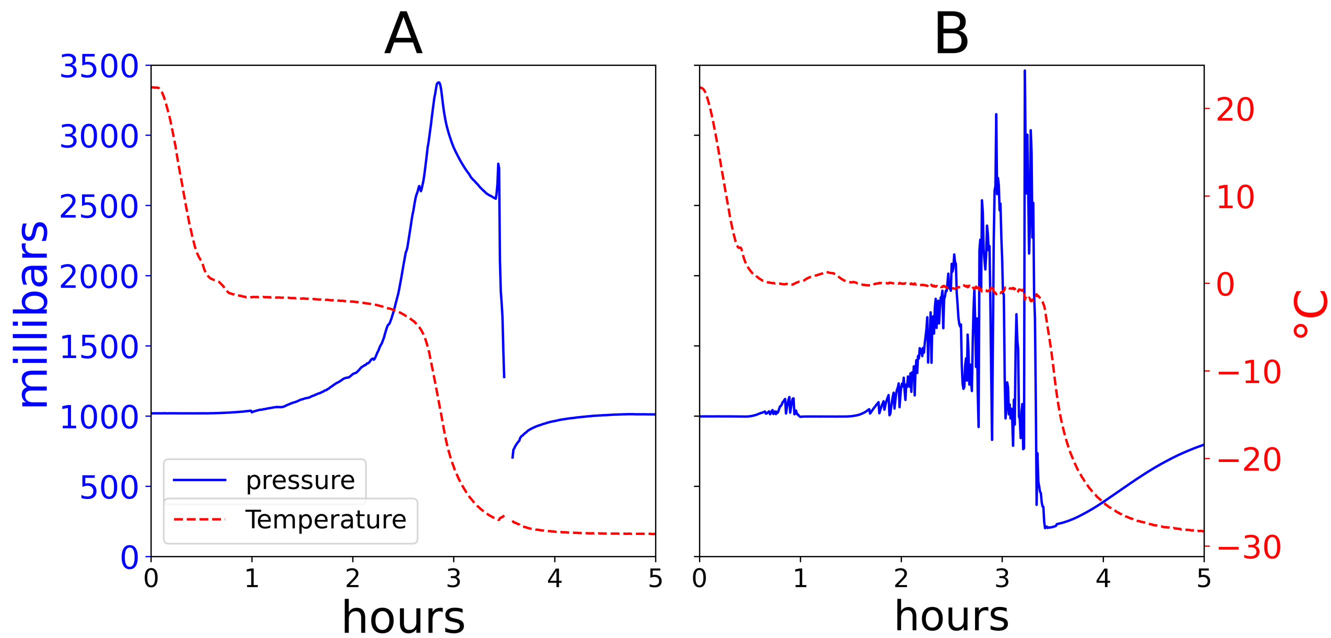

Fig. 3. In situ temperature and pressure during freezing, demonstrating difference between saltwater and freshwater experiments. A. Experiment with set point temperature -30 °C and salinity 6 g/L. B. Experiment with set point temperature -30 °C and salinity 0 g/L.

Image and video observations

Visual inspection of videos taken by the borescope reveal both deformation and fracture over the course of experiments. As the pressure begins to rise, the ice deforms and the plastic bag expands. We observe deformation that is greatest at the center of the top surface of the bag, with diminishing deformation radially away. In freshwater experiments, we observe accelerated ice deformation with increasing pressure until fractures develop. After fracture, less deformation is apparent. In saltwater experiments, the same process occurs without fractures. No deformation is observed after freezing is complete. Freezing is also accompanied by an ice opacity decrease from clear to cloudy over the scale of half an hour.

Temperature and salinity dependence

We find that colder temperatures and lower salinities are systematically associated with fracturing. Our results show the existance of two distinct regimes that occur above and below a critical temperature of approximately -20° C (Figure 4). In the high temperature regime between -5° C and -20° C the temperature-salinity (TS) boundary between fractured and unfractured ice is nearly vertical, indicating low temperature sensitivity. In the low temperature regime below -20° C, a strong temperature dependence is observed.

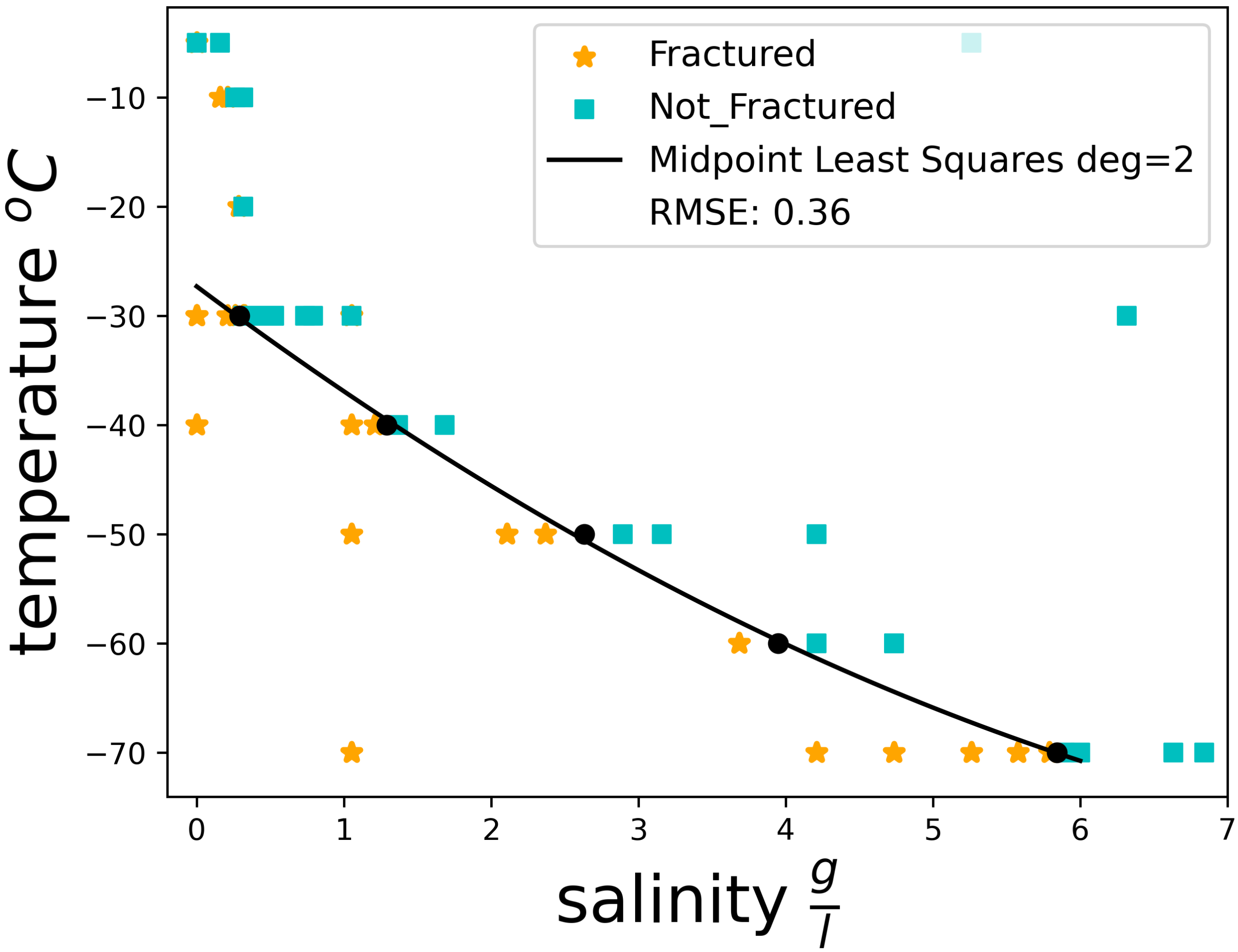

Fig. 4. The fracture stability TS curve. Orange stars show experiments where fractures were present and teal squares show experiments where fractures were absent. For each temperature where experiments were conducted, the black circles denote the midpoint between the salinities where fractures were and were not observed; the black curve connects the black dots with a parabolic polynomial.

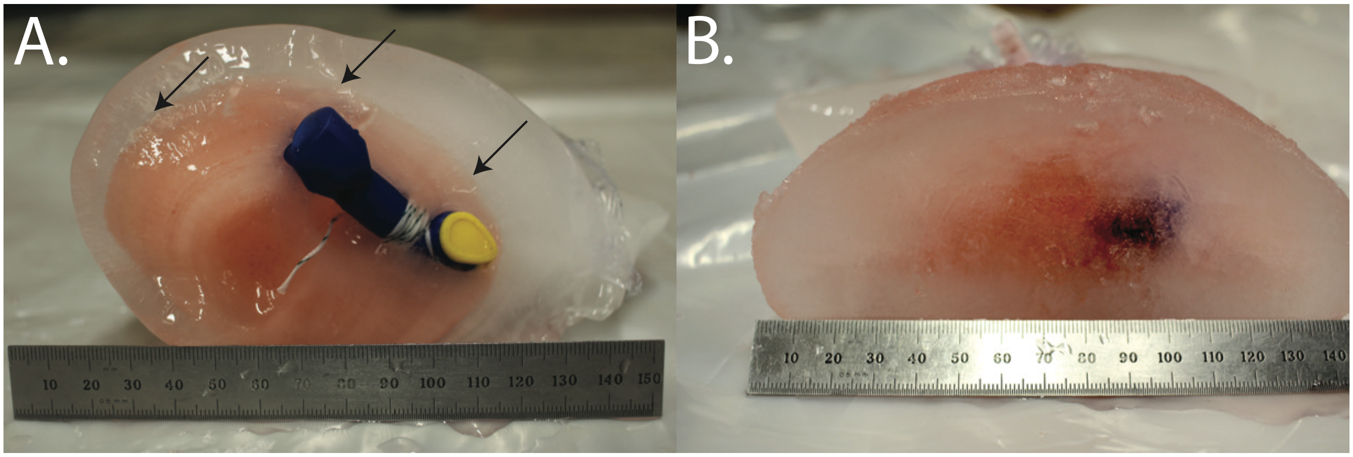

Fig. 5. Samples after freezing and saw cut in cross section. A. Set point temperature -60 °C, freshwater; B. Set point temperature -10°C; salinity 5 g/l. The freshwater sample shows a region without dye with a sharp boundary (noted with black arrows). The saltwater sample shows a diffuse gradient between regions with higher and lower dye concentrations.

Diffusion of dye

We find that the dye injected into freshwater experiments remains concentrated, freezing with no diffusion into existing ice (Figure 5 A). Dye injected into saltwater experiments diffuses through ice forming a homogeneous diffuse distribution of dye through the sample (Figure 5 B). When sawing cross sections, freshwater experiments were notably more brittle than salty experiments, though this may be partially attributable to other factors that were not carefully controlled in our lab space such as the ambient temperature.

DISCUSSION

Our main result is that the addition of NaCl to freshwater creates a brittle-to-ductile transition during freezing. In freshwater samples, large fractures on the scale of the sample were found using both direct visual at the conclusion of the experiment as well as boroscope video during the experiment. Smaller fractures are not easily discernible to the eye, but are interpreted to be observed through the occurrence of rapid pressure oscillations (Figure 3b). We interpret these rapid pressure oscillations as being due to water pressure drops that occur when pressurized water in the central unfrozen region breaks through the icy shell and re-equilibrates with the pressure due to the confining plastic bag. The addition of NaCl salt, at concentrations of a few g/L, prevents the occurrence of both large and small fractures.

We now construct a set of simple physical models to explain our results. The main conclusion from these models is that the brittle-ductile transition in our experiments occurs due to poroelastic effects. We find that increasing the salinity in our samples creates an interconnected briny pore space that allows pressure diffusion and limits water pressures below those required to instigate fracture.

We begin by examining a model of the plastic bag as a thin, pressurized spherical shell (Section). We then consider a model that captures water pressure while assuming that ice remains linear elastic (Section), and we see that this assumption predicts unphysically large stresses. We also consider a linear viscoelastic ice rheology, but conclude that no reasonable parameter choices are able to match observed water pressures. In Section we consider thermodynamic effects and see that while thermodynamic considerations accurately predict the time evolution of the frozen fraction, they do not act to limit water pressure. Finally, in Section we consider poroelastic effects.

Model preliminaries

We first introduce the setting and notation for our models. Our models all involve an initially spherical volume of water that grows radially to a new volume upon complete freezing. The initial radius of the spherical sample is located at $r = R$ with radial coordinate r. We calculate the change in radius as the sphere grows to a new value $R + u$ associated with the volumetric strain from freezing,

$$1 + \gamma \equiv \frac{(V_0 + \Delta V)}{V_0} = \left(\frac{R+u}{R}\right)^3 = \frac{\rho_i}{\rho_w} \approx 1.1. \tag{1}$$

Solving for the displacement of the outer boundary, we find that $u \approx 0.03R$. The radius of the icy sphere is therefore about 3% greater than the radius of the sphere of liquid water.

The momentum balance equation in spherical coordinates and assuming spherical symmetry is,

$$\frac{\partial \sigma_{rr}}{\partial r} + \frac{2(\sigma_{rr} - \sigma_{\theta\theta})}{r} = 0 \tag{2}$$

We use a spherical coordinate system with coordinates r, θ, and ψ. The Cauchy stress components and the pressure are given by,

$$\sigma^{rr} = E_* \left[(1-\nu)\frac{du}{dr} + 2\nu\frac{u}{r} \right] \tag{3}$$

$$\sigma^{\theta\theta} = \sigma^{\psi\psi} = E_* \left[\nu\frac{du}{dr} + \frac{u}{r} \right] \tag{4}$$

We introduce the convenience variable $E_* \equiv E/[(1+\nu)(1-2\nu)]$ where E and ν are the Young's modulus and Poisson ratio.

The general solution to Equations 2-4 is (Bower, 2014, p. 198),

$$u = c_1 r + \frac{c_2}{r^2} \tag{5}$$

Where c_1 and c_2 are constants that are determined by boundary conditions. By modifying these boundary conditions, we model two different physical processes. First, we use Equation 5 to model the stiffness imparted by the elasticity of the plastic bag (Section). Then, we later use it to model the radial stress distribution in the ice itself (Section).

Model of the plastic bag as a thin elastic shell

Model

Given a prescribed volumetric strain $\gamma = 0.1$ due to the phase transition (Equation 1), we now calculate how much stiffness is imparted upon the ice due to the confinement of the ice by the plastic bag. We model the plastic bag as a thin flexible shell using Equation 5 with the following boundary conditions. The inner surface of the plastic bag is located at $r = R$ and the outer edge is located at $r = R + h$, where h is the thickness of the plastic bag. Relating the displacement and pressure at the outer boundary and taking the limit of thin shell thickness $h \ll R$, results in an expression for the effective compliance of the shell β,

$$u = \frac{R^2 f(\nu)}{2E_* h} p \equiv \beta p \tag{6}$$

where the function $f(\nu) = (1+\nu)/(3\nu+1)$ takes on the value $f(\nu = 0.3) = 0.68$. We note that equation 6 is in the form of a Robin-type boundary condition that relates pressure to displacement, with β acting as the effective compliance of the plastic bag.

Analysis of Experiments

For our plastic bags, we estimate the thickness $h = 50$ μm, $E = 500$ MPa, and $\nu = 0.3$. We assume that one liter of water occupies a sphere with radius $R \approx 6.2$ cm that grows by an amount $u \approx 1.9$ mm giving an effective modulus $1/\beta \approx 36$ MPa/m and corresponding pressure $p \approx 1.7$ bar. This value is slightly lower than the observed ~ 3.5 bar pressure. This mismatch likely occurs because our samples are not perfectly spherical.

Model of volume change during freezing as a transformation strain

Model

We consider a two layer system that consists of a central sphere of liquid water surrounded by an ice shell. The central sphere of liquid water has radius R_i and volume $V_{liquid} = \frac{4}{3}\pi R_i^3$. The outer extent of the ice shell is at $r = R$, implying an ice volume $V_{ice} = \frac{4}{3}\pi(R^3 - R_i^3)$. The total volume of the system is $V_0 = \frac{4}{3}\pi R^3$. The volume fraction of ice is $\phi = \frac{V_i}{V_0}$ and the volume fraction of water is $1 - \phi$.

In Section we were able to treat the volumetric strain due to freezing γ as a boundary condition acting on the confining plastic bag. We now need to model a continuum volumetric strain that is distributed throughout the ice layer. In particular, the volume change during freezing enters the solution by way of the constitutive relation. The basic idea is that even in the absence of stress, the phase change induces a strain in newly frozen ice. Schematically, an elastic constitutive relation of the form $\sigma = k\epsilon$ is replaced with one of the form $\sigma = k(\epsilon - \gamma)$, recalling that γ is the transformation strain associated with the phase change

(Eshelby, 1957). Adapting this simplified model to the tensorial constitutive relation gives,

$$\sigma_{rr} = E_* \left[(1-\nu_i) \frac{\partial u_i}{\partial r} + 2\nu_i \frac{u_i}{r} - \gamma \right] \tag{7}$$

$$\sigma_{\theta\theta} = \sigma_{\psi\psi} = E_* \left[\nu \frac{du}{dr} + \frac{u}{r} - \gamma \right], \tag{8}$$

where γ is the volumetric strain defined in Equation 1.

The general solution of Equation 5 now applies in both the liquid water and the ice phase, resulting in a system with four constants to be determined from boundary conditions. Technically we are able to use the general solution despite the presence of the transformation strain in Equations 7 and 8 because γ does not vary spatially, therefore cancels out when Equations 7 and 8 are substituted into the statement of momentum balance in Equation 2. The boundary conditions are,

$$|u(r=0)| < \infty \tag{9}$$

$$u(r=R_I^+) = u(r=R_I^-) \tag{10}$$

$$\sigma_{rr}(r=R_I^+) = p_\ell(R_I^-) \tag{11}$$

$$\sigma_{rr}(r=R) = 0 \tag{12}$$

where the water pressure is,

$$p_\ell = \frac{1}{3}\left(\sigma_{rr}^\ell + \sigma_{\theta\theta}^\ell + \sigma_{\phi\phi}^\ell\right) = K_\ell \left[\frac{du}{dr} + 2\frac{u}{r} \right] \tag{13}$$

with liquid water bulk modulus K_ℓ. We could have used Equation 6 instead of a stress free outer boundary, but we focus here first on the simpler system.

Descriptively, the first condition (Equation 9) requires bounded displacements at the origin. The second and third conditions (Equation 10 and 11) reflect continuity of displacements and momentum across the ice/water interface. The final condition (Equation 12) requires zero stress at the outer edge of the ice. The latter boundary condition could be replaced with a spring boundary to represent a container, but we will see later that this is not an important feature to include because the stiffness of a thin plastic layer is dwarfed by the stiffness of the ice.

We express the water pressure during freezing in terms of the effective modulus M and the transformation

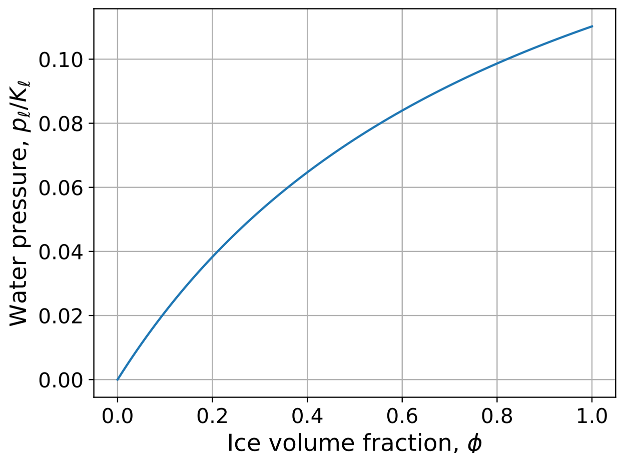

Fig. 6. Water pressure within an unfrozen sphere of liquid water surrounded by an expanding icy shell, given as a function of ice volume fraction.

strain γ as,

$$p_\ell = \gamma M(\phi) \tag{14}$$

Here, the effective modulus M accounts for the relative stiffness of water and ice, as well as the spherical geometry. It accounts for the idea, common in multiphase systems, e.g., (Lipovsky and Dunham, 2016), that more deformation is accompanied in the more compliant material. It is given by,

$$M(\phi) = \frac{6E_* K_\ell \phi}{5K_\ell \left[\kappa + 2(1-\phi)\right] + 2E_* \kappa \phi}, \tag{15}$$

where for convenience we have introduced $\kappa = 3\nu + 1$. Equation 15 is plotted in Figure 6.

In the limit that the ice is a thin shell surrounding the liquid phase, $\phi \ll 1$, M attains the limit,

$$M(\phi) = \frac{6E_*\phi}{5(\kappa+2)} \equiv E_0\phi. \tag{16}$$

where $E_0 \approx 5$GPa is the effective rigidity in this limit.

Analysis of experiments

The most important feature of this model is that it predicts stresses high enough to induce fracture after only a small amount of freezing. Consider, for example, a modest initial flaw in the ice with $L = 1$ mm length scale. This flaw is expected to nucleate a propagating fracture when $p_\ell = \frac{K_{Ic}}{\sqrt{\pi L}}$ where K_{Ic} is the fracture toughness (Van der Veen, 1996; Lipovsky, 2020). Realistic fracture toughness values for ice $K_{Ic} \approx 100$ kPa$\sqrt{\text{m}}$ imply fracture growth with a water pressure $p_\ell \sim 0.5$ bar. In our model, such stresses are reached when $\phi = 10^{-5}$. Even a small amount of freezing therefore generates high enough water pressure to fracture the shell.

The results of the previous section are easily extended to the case of a linear viscoelastic ice shell using the viscoelastic correspondence principal (Cathles, 2015; Lipovsky, 2022). The main result of this analysis, however, is that physically realistic values of the viscosity of salty ice cannot possibly account for the observed water pressure evolution. Using reported values for the effective viscosity of saline ice (Schulson and Duval, 2009, Ch. 13), we calculate that our experiments occur over shorter durations than the Maxwell time of ice. For this reason, we do not expect viscoelastic effects to be important.

Thermodynamics

Model

So far we have only modeled the pressure at a given ice fraction, but we have not yet described the evolution of that ice fraction. In this section we describe that evolution. We ignore the pressure dependence on the melting point because our experimental data suggest that this is not a large effect. We consider heat conduction in a spherical shell under the assumption of spherical symmetry. We assume the inner boundary of the shell is at the melting point and the outer boundary has a prescribed heat flux. In steady state the temperature profile is,

$$T(r) = \frac{QR}{k_I} \log\left(\frac{r}{R_I}\right), \tag{17}$$

where k_I is the thermal conductivity of ice. The rate of migration of the ice front toward the origin is then given by,

$$\dot{R}_I(t) = \frac{k_I(\partial T/\partial r)\big|_{r=R_I}}{\rho L_f} = \frac{Q}{\rho L_f}\frac{R}{R_I}, \tag{18}$$

which shows that the rate of ice front growth is fastest when the ice is almost completely frozen. Integrating then gives,

$$\frac{R_I(t)}{R} = \sqrt{1 - \frac{t}{t_f}} \tag{19}$$

where $t_f = \rho L_f R/(2Q)$ is the time required to freeze the sample with L_f denoting the latent heat of fusion of ice.

Analysis of experiments

We estimated the heat flux Q by examining the temperature curve during the initial period of specific cooling, prior to the onset of the freezing phase transition. The total heat lost from the sample during this time is $q = mc\Delta T$, with sample mass $m = 1$ kg, specific heat of liquid water $c = 4186$ J/kg, and temperature change $\Delta T \approx 20°$C, or $q \approx 83.7$ kJ. The heat flux is $Q = q/(A\Delta t)$, with surface area A and duration of cooling Δt. Assuming cooling occurred over 30 minutes (i.e., as observed in the experiments in Figure 3) and sample area of 0.067 m^2 gives a heat flux of 694 W/m^2. From Equation 19, the expected freezing time is then ~ 5.5 h, comparable in order-of-magnitude, but overestimating the observed freezing time ~ 2.5 h. The deviation from our model and experiment likely reflect the shortcomings of our spherical model geometry, and are therefore useful to gauge the effect of this assumption.

Poroelastic effects

Model

A number of studies have examined the dynamics of brine flow through an icy matrix using an idealized Hele-Shaw cell approach (Worster, 1997; Ding and others, 2019; Parkinson and others, 2020). Here, in order to capture the elastic stresses that mediate fracture propagation, we use a poroelastic framework of the mushy layer, similar, for example, to magma chamber studies (Liao and others, 2021, 2018). Specifically, we extend the model developed by Verruijt (2013) for solving Cryer's problem to describe our situation with flow of salty water through a poroelastic ice matrix. Momentum balance in the radial direction is given by Equation 2. We then introduce the effective stresses,

$$\sigma_{rr} = \sigma'_{rr} + \alpha p \tag{20}$$

$$\sigma_{\theta\theta} = \sigma'_{\theta\theta} + \alpha p \tag{21}$$

where R is the radial coordinate and σ_{rr} and $\sigma_{\theta\theta}$ are the total stresses in radial and tangential directions. The momentum balance equation can then be written in terms of the effective stresses as,

$$\frac{\partial \sigma'_{rr}}{\partial r} + 2\frac{\sigma'_{rr} - \sigma'_{\theta\theta}}{r} = -\alpha \frac{\partial p}{\partial r} \tag{22}$$

The effective stresses σ'_{rr} and $\sigma'_{\theta\theta}$ are related to strain and displacement through,

$$\sigma'_{rr} = -\left(K - \frac{2}{3}G\right)\epsilon - 2G\frac{\partial u}{\partial r} \tag{23}$$

$$\sigma'_{\theta\theta} = -\left(K - \frac{2}{3}G\right)\epsilon - 2G\frac{u}{r} \tag{24}$$

$$\epsilon = \frac{\partial u}{\partial r} + \frac{2u}{r} = \frac{1}{r^2}\frac{\partial (ur^2)}{\partial r} \tag{25}$$

The equations are closed through mass conservation, which follows the coupled diffusion equation,

$$\alpha \frac{\partial \epsilon}{\partial t} + S\frac{\partial p}{\partial t} = \frac{k}{\gamma}\left(\frac{\partial^2 p}{\partial r^2} + \frac{2}{r}\frac{\partial p}{\partial r}\right). \tag{26}$$

The boundary conditions on the inner edge of the shell, $R = R_i$, are,

$$\sigma'_{rr} = 0 \tag{27}$$

$$p = p_w(t) \tag{28}$$

and the boundary conditions on the outer edge of the shell $r = R$, are,

$$\sigma'_{rr} = 0 \tag{29}$$

$$\partial p/\partial r = 0. \tag{30}$$

We solve equations 20 to 30 using a finite difference scheme with explicit time stepping. We then employ this solver to simulate the pressure difference from the liquid-ice boundary through a partially frozen spherical ice shell under various permeabilities (Figure 7).

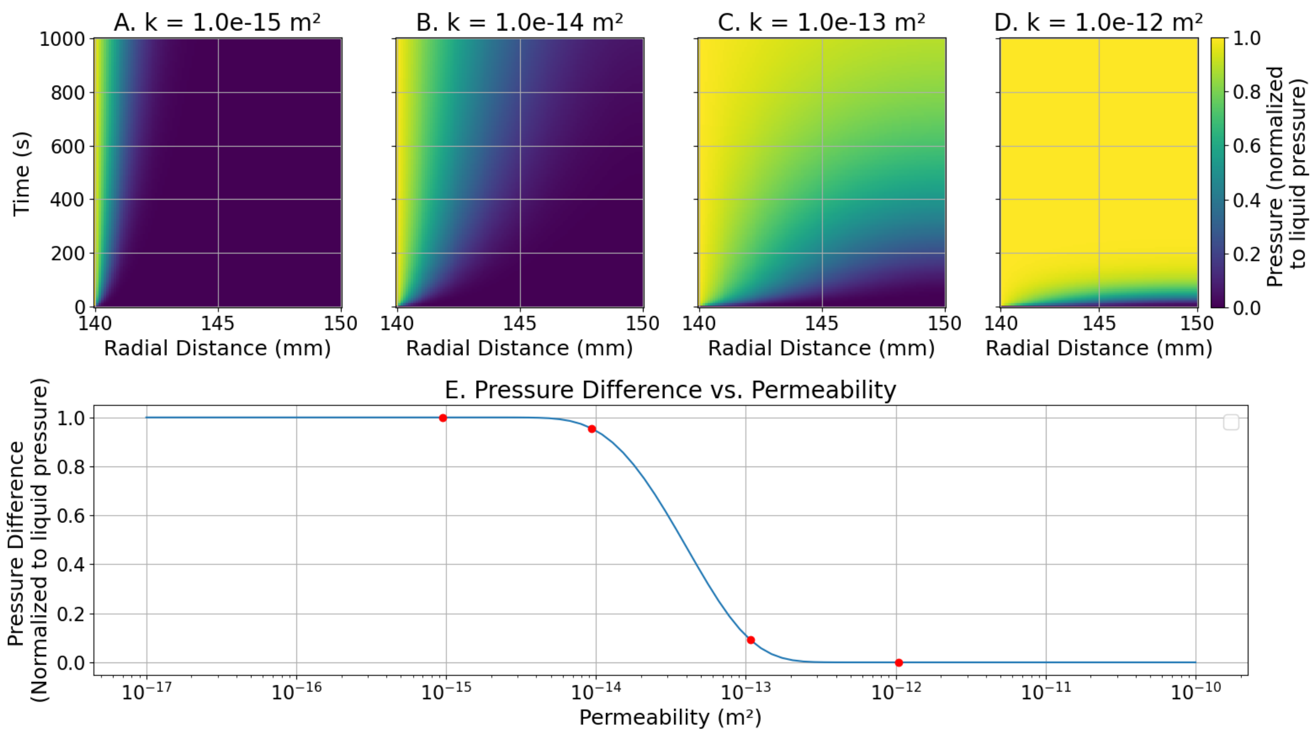

Fig. 7. A-D. Numerical calculations of the water pressure in a poroelastic ice shell with different hydraulic permeabilities. The liquid phase region extends from 0 mm to 140 mm and the ice shell comprises 140 mm to 150 mm. E. pressure differences at the last time step between the liquid-ice boundary at 140 mm and the outer shell boundary at 150 mm as a function of permeability. The red dots indicate the four regimes of permeability shown in panels A-D in sequential order.

Analysis of experiments

Porosity is more easily observed than permeability, yet permeability offers more direct influence on hydraulic dynamics. For this reason, hydromechanical studies often seek porosity-permeability relationships to relate the two. We estimate the porosity by estimating the unfrozen brine fraction as a function of temperature following Weeks and Ackley (1982). At -5°C unfrozen brine exists with salinity 80 per mil by weight (Weeks and Ackley, 1982). The brine volume V_b that supports this salinity, based on an initial (room temperature) 5 g/L salt content, is $V_b = 0.06$ L. The brine volume fraction, for a total frozen volume $V_0 + \Delta V \approx$1.1 L, the resulting porosity is $\phi = V_b/(V_0 + \Delta V) \approx 0.057$. At -10°C the porosity is $\phi \approx 0.032$ and at -20°C it is $\phi \approx 0.020$.

We calculate permeability by tuning this value in our numerical model to match the observation that pressure is able to diffusive through the ice sample. We assume a 10 mm thick ice layer to simulate the initial fracturing that we observe early in the freezing process. We find that there exists a critical permeability region between 10^{-14} and 10^{-13} m^2. In the less permeable regime (less than 10^{-14}m^2), the pressure difference through the shell is maximal. In permeabilities greater than this, the pressure difference drops extremely rapidly to effectively zero. Greater permeabilities can be achieved through the inclusion of salt in the water, which forms brine channels and pockets.

We therefore conclude that, for porosities in the range of $\phi = 0.02$ to 0.06, the permeability of our samples had to be at least 10^{-14} m^2. This is a lower bound on the permeability since our model is only able to estimate when pressure diffusion first becomes possible as a function of permeability. These values are consistent with previous studies. The study by Maus and others (2020), for example, found a sea ice permeability of 10^{-14} to 10^{-11} m^2 for brine porosities in the range of $\phi = 0.02$ to 0.03.

One fundamental limitation of our work is that we are limited to the inwards freezing pattern in order to create the pressure difference that drives fracture. This inwards freezing pattern results in a specific ice crystal structure that may or may not be representative of sea ice or marine ice in natural settings. This limitation may be a minor one, however, given the consistency highlighted above with the work of (Maus and others, 2020).

Our low temperature results are consistent with this analysis. Ice-NaCl reaches a eutectic point in the form of pure water ice + solid NaCl 2H2O at -21.2 °C (Weeks and Ackley, 1982). Although we conducted experiments with set point temperature below the eutectic temperature, we still expect the above poroelastic diffusion mechanism to operate at these low temperatures because fluid can flow through the ice matrix for some time before the channels reach the eutectic point. This enables salty experiments frozen at very cold temperatures to exhibit porous behavior during the freezing process and resist fracture (Figure 4).

We observe a transition in our experiments for experiments conducted at the eutectic temperature. Experiments with set point temperature below the eutectic point exhibit a brittle–ductile transition that occurs at higher salinity with decreasing temperature(Figure 4). Even in experiments at set-point temperatures approaching -70 $^{\circ}C$, we expect that brine channels freeze after the end of an experiment as the ice temperature fully equilibrates with the set point temperature. We expect that the salinity dependence of the brittle–ductile transition at these lower set point temperatures occurs because of the same general principle as at higher temperatures: because higher salinities enable a greater brine volume and therefore higher permeabilities. These effects become more pronounced at lower temperatures as the outermost part of the shell completely freezes and requires a higher salt content to keep brine channels open over the time period required for the sample to completely freeze.

CONCLUSIONS: IMPLICATIONS FOR FRACTURES IN ICE SHELVES AND BEYOND

We used a simple experimental setup and physical models to understand the brittle-ductile transition in NaCl water ice as a function of temperature and salinity. Our results provide a physical mechanism that explains the observation that suture zones arrest rift propagation in the Antarctic ice shelves. Specifically, it suggests that accreted marine ice arrests rift propagation because its elevated salinity content creates a poroelastic response that allows water pressure diffusion. This type of behavior, where additional forces act in the tip region of a propagating crack, is commonly referred to as a cohesive zone (Palmer and Rice, 1973) and has previously been inferred to act during ice shelf rift propagation (Lipovsky, 2018). Such behavior is consistent with previous studies that demonstrated high sensitivity of rift propagation to small perturbations in ocean water pressure along rift walls (Olinger and others, 2024). Beyond marine ice sheets, our experiments and analysis likely has further application in the study of sea ice deformation processes and in the warmer, deeper extents of fracture zones in planets with icy shells.

ACKNOWLEDGEMENTS

We would like to thank Michael McCarthy for assistance with using an environmental chamber. Sasha Seroy provided assistance with MicroPython pressure sensor code. Caleb Flaim helped with assembling pressure sensors. Alexandre Lipovsky helped with the early experiments. This work benefited from a discussion with Andrew Wells and Sylvain Marseille. This work was supported by the National Science Foundation through award #2213705.

REFERENCES

Borstad C, McGrath D and Pope A (2017) Fracture propagation and stability of ice shelves governed by ice shelf heterogeneity. *Geophysical Research Letters*, **44**(9), 4186–4194.

Buffo J, Meyer C and Parkinson J (2021) Dynamics of a solidifying icy satellite shell. *Journal of Geophysical Research: Planets*, **126**(5), e2020JE006741.

Cathles LM (2015) *Viscosity of the Earth's Mantle*, volume 1362. Princeton university press.

Chen C, Zhang H, Liu S, Jin C, Chen Y, Zhang N and Talalay P (2019) Hydraulic fracturing in ice boreholes: theory and tests. *Polar Science*, **19**, 40–48.

Craven M, Allison I, Fricker HA and Warner R (2009) Properties of a marine ice layer under the amery ice shelf, east antarctica. *Journal of Glaciology*, **55**(192), 717–728.

Ding GY, Wells AJ and Zhong JQ (2019) Solidification of binary aqueous solutions under periodic cooling. part 1. dynamics of mushy-layer growth. *Journal of Fluid Mechanics*, **870**, 121–146 (doi: 10.1017/jfm.2019.256).

Eshelby JD (1957) The determination of the elastic field of an ellipsoidal inclusion, and related problems. *Proceedings of the royal society of London. Series A. Mathematical and physical sciences*, **241**(1226), 376–396.

Fu P, Schoenball M, Ajo-Franklin JB, Chai C, Maceira M, Morris JP, Wu H, Knox H, Schwering PC, White MD and others (2021) Close observation of hydraulic fracturing at egs collab experiment 1: Fracture trajectory, microseismic interpretations, and the role of natural fractures. *Journal of Geophysical Research: Solid Earth*, **126**(7), e2020JB020840.

Jansen D, Luckman A, Kulessa B, Holland PR and King EC (2013) Marine ice formation in a suture zone on the larsen c ice shelf and its influence on ice shelf dynamics. *Journal of Geophysical Research: Earth Surface*, **118**(3), 1628–1640.

Kulessa B, Booth AD, O'Leary M, McGrath D, King EC, Luckman AJ, Holland PR, Jansen D, Bevan SL, Thompson SS and others (2019) Seawater softening of suture zones inhibits fracture propagation in antarctic ice shelves. *Nature Communications*, **10**(1), 5491.

Liao Y, Soule SA and Jones M (2018) On the mechanical effects of poroelastic crystal mush in classical magma chamber models. *Journal of Geophysical Research: Solid Earth*, **123**(11), 9376–9406.

Liao Y, Soule SA, Jones M and Le Mével H (2021) The mechanical response of a magma chamber with poroviscoelastic crystal mush. *Journal of Geophysical Research: Solid Earth*, **126**(4), e2020JB019395.

Lipovsky B and Dunham E (2016) Tremor during ice-stream stick slip. *The Cryosphere*, **10**(1), 385–399.

Lipovsky BP (2018) Ice shelf rift propagation and the mechanics of wave-induced fracture. *Journal of Geophysical Research: Oceans*, **123**(6), 4014–4033.

Lipovsky BP (2020) Ice shelf rift propagation: stability, three-dimensional effects, and the role of marginal weakening. *The Cryosphere*, **14**(5), 1673–1683.

Lipovsky BP (2022) Density matters: ice compressibility and glacier mass estimation. *Journal of Glaciology*, **68**(270), 831–832 (doi: 10.1017/jog.2021.132).

Maus S, Schneebeli M and Wiegmann A (2020) An x-ray micro-tomographic study of the pore space, permeability and percolation threshold of young sea ice. *The Cryosphere Discussions*, **2020**, 1–30.

McCarthy C, Cooper RF, Kirby SH, Rieck KD and Stern LA (2007) Solidification and microstructures of binary ice-i/hydrate eutectic aggregates. *American Mineralogist*, **92**(10), 1550–1560.

McGrath D, Steffen K, Holland PR, Scambos T, Rajaram H, Abdalati W and Rignot E (2014) The structure and effect of suture zones in the larsen c ice shelf, antarctica. *Journal of Geophysical Research: Earth Surface*, **119**(3), 588–602.

Olinger SD, Lipovsky BP and Denolle MA (2024) Ocean coupling limits rupture velocity of fastest observed ice shelf rift propagation event. *AGU Advances*, **5**(1), e2023AV001023.

Palmer AC and Rice JR (1973) The growth of slip surfaces in the progressive failure of over-consolidated clay. *Proceedings of the Royal Society of London. A. Mathematical and Physical Sciences*, **332**(1591), 527–548.

Parkinson JR, Martin DF, Wells AJ and Katz RF (2020) Modelling binary alloy solidification with adaptive mesh refinement. *Journal of Computational Physics: X*, **5**, 100043.

Schulson and Duval (2009) Creep and fracture of ice. *Journal of Glaciology*, **57**(202), 325–328 (doi: 10.3189/S0022143000206254).

Schulson EM and Renshaw CE (2022) Fracture, friction, and permeability of ice. *Annual Review of Earth and Planetary Sciences*, **50**(1), 323–343.

Van der Veen C (1996) Tidewater calving. *Journal of Glaciology*, **42**(141), 375–385.

Vance S, Hand K and Pappalardo R (2016) Geophysical controls of chemical disequilibria in europa. *Geophysical Research Letters*, **43**(10), 4871–4879.

Verruijt A (2013) Theory and problems of poroelasticity. *Delft University of Technology*, **71**, 465.

Weeks WF and Ackley SF (1982) The growth, structure, and properties of sea ice. *No source information available*, 5.

Wolfenbarger NS, Fox-Powell MG, Buffo J, Soderlund KM and Blankenship DD (2022) Brine volume fraction as a habitability metric for europa's ice shell. *Geophysical Research Letters*, **49**(22), e2022GL100586.

Worster MG (1997) Convection in mushy layers. *Annual Review of Fluid Mechanics*, **29**(1), 91–122.

Yuan C, Cochard T, Denolle M, Gomberg J, Wech A, Xiao L and Weitz D (2024) Laboratory hydrofractures as analogs to tectonic tremors. *AGU Advances*, **5**(1), e2023AV001002.